JOURNAL OF SPACECRAFT AND ROCKETS
Vol. 41, No. 4, July–August 2004

Electric Field, Magnetic Field, and Density Measurements on the Active Plasma Experiment

Robert F. Pfaff,* Henry T. Freudenreich,† and Scott R. Bounds‡
NASA Goddard Space Flight Center, Greenbelt, Maryland 20771
Peter A. Delamere§
University of Colorado, Boulder, Colorado 80309
Robert E. Erlandson¶ and Cheng I. Meng**
Johns Hopkins University, Applied Physics Laboratory, Laurel, Maryland 20723
and
Julius I. Zetzer††and Boris G. Gavrilov‡‡
Institute of Geospheres Dynamics, 117334, Moscow, Russia

High-resolution, in situ measurements of dc and wave electric fields, magnetic fields, and plasma number density have been gathered by instruments on a diagnostic payload at which a high-velocity, overdense aluminum ion beam was directed from a separate payload spaced 468 m away. The experiment, called the Active Plasma Physics Experiment, was carried out in the Earth's high-latitude ionosphere at 360-km altitude using a sounding rocket. The experimental data clearly show a large diamagnetic cavity with a 93% depletion of the Earth's magnetic field within a narrowly confined (<500-m) ion beam whose number density exceeded 10^9 cm^{-3}. Associated with the release, dc electric fields with amplitudes >1.5 V/m perpendicular to the magnetic field were observed that represented both the $\boldsymbol{E} \times \boldsymbol{B}$ bulk plasma velocity and a magnetosonic wave, which preceded the arrival of the beam that was also evident in the ΔB magnetometer data. The electric field data also show the presence of electric fields parallel to the magnetic field, including a bipolar electric field signature presumably set up to ensure current continuity. Other plasma waves associated with the release include Alfvén perturbations, intense broadband turbulence extending to frequencies beyond 1 MHz, whistler-mode electromagnetic emissions at the ambient O^+ lower hybrid frequency, and ion acoustic turbulence. The measurements provide a self-consistent picture of the electrodynamics surrounding a high-velocity, overdense ion beam released in the high-latitude ionosphere.

Nomenclature

Al^+	=	aluminum ion
Al^{++}	=	double-ionized aluminum
$\boldsymbol{B}$	=	magnetic field vector
$B_\perp$	=	magnetic field component perpendicular to the ambient magnetic field
$B_\parallel$	=	magnetic field component parallel to the ambient magnetic field
$\boldsymbol{E}$	=	electric field vector
$E_\perp$	=	electric field component perpendicular to the magnetic field
$E_\parallel$	=	electric field component parallel to the magnetic field
$\boldsymbol{E} \times \boldsymbol{B}$	=	electric field cross magnetic field, velocity
$\boldsymbol{J}$	=	conduction current
K_B	=	Boltzmann constant
n	=	number density, cm^{-3}
O^+	=	oxygen ion
T	=	plasma temperature
T_e	=	electron temperature
T_i	=	ion temperature
ΔB	=	magnetic field variation
ΔE	=	electric field variation
$\Delta \boldsymbol{E} \times \Delta \boldsymbol{B}$	=	electric field variation cross magnetic field variation, velocity
ΔN	=	perturbed number density, cm^{-3}
μ_0	=	permeability of free space

Received 26 March 2003; revision received 30 September 2003; accepted for publication 10 October 2003.

*Space Scientist.
†Research Scientist, L3 Comm.
‡Research Associate; currently Research Scientist, University of Iowa, Iowa City, IA 52242.
§Research Associate, Laboratory for Atmospheric and Space Physics.
¶Group Supervisor.
**Branch Supervisor.
††Deputy Director.
‡‡Head, Laboratory for Magnetosphere-Earth Coupling.

Introduction

THE natural space environment can be characterized as a slowly varying medium that is sometimes abruptly interrupted by beams of particles that travel at high speeds relative to the ambient gas. Examples include comets, energetic auroral beams, meteors, and plumes from eruptions such as on Jupiter's moon, Io. "Controlled" experiments that initiate such beam-like perturbations in space, and for which the initial conditions and experiment parameters are known with a high degree of confidence, provide opportunities to significantly advance our understanding of the interactions of such beams with the space environment.

High-speed, localized plasma beams or jets in the Earth's ionosphere involve a complex electrodynamics that exist on highly confined time and distance scales. Such electrodynamics includes currents and electric fields associated with localized packets of plasma that may be sufficiently dense to create and sustain self-contained diamagnetic cavities. The Active Plasma Experiment (APEX)[1] provides an excellent opportunity to further our understanding of the electrodynamics surrounding such high-speed, evolving ion beams and their associated diamagnetic cavities in the Earth's ionosphere.

This paper presents in situ data gathered on the APEX sounding rocket payload that include measurements of the electric fields, magnetic perturbations and currents, plasma density, and plasma waves

ranging in frequency between dc and 2.5 MHz. These data reveal the interdependency of the electric fields, currents, and plasma density variations associated with a high-density aluminum vapor release in the Earth's high-latitude ionosphere that underwent extremely rapid ionization. Additionally, these same measurements were also used to establish the background geophysical plasma conditions in which the release was conducted.

Several previous experiments have also explored the electrodynamics of controlled high-velocity, ionized beams in the Earth's ionosphere. For example, in the CRIT I experiment Kelley et al.[2] showed that a large, quasi-dc electric field was detected antiparallel to a beam of barrium particles with a large-amplitude, highly localized parallel electric field component that compared well with a theoretical model.[3] A second experiment, CRIT II, produced benchmark observations important for the evaluation of Alfvén's critical velocity effect[4] along with a complicated electrodynamic and plasma wave structure.[5] Other rocket release experiments whose results address these physical problems include the Condor experiment[6] and Porcupine experiments.[7]

As will be shown in this paper, the data gathered during the APEX experiment reveal a complex electrodynamics associated with a high-speed, aluminum ion beam release in the high-latitude ionosphere. When analyzed in conjunction with the onboard photometer, energetic particle, and other measurements, these data enhance considerably our understanding of the spatial and temporal electrodynamics inherent to a high-speed, overdense aluminum ion beam in the Earth's ionosphere.

Experiment Description

The APEX experiment consisted of four payloads launched on a single NASA Black Brant XII rocket from Poker Flat, Alaska. The payloads consisted of two explosive-type generators (ETG1, ETG2), a plasma diagnostics payload (PDP), and an optical sensor payload. The launch was carried out at 13:57:03 UT on 22 January 1999. Apogee was 364 km, occurring at 353.6 s after launch. The first release occurred just before apogee at an altitude of 360 km. The second release occurred at 280-km altitude on the downleg. Details of the overall experiment can be found in Erlandson et al.[1] This paper discusses data from the first release only.

For the first release, the beam was directed at the PDP payload situated 468 m away. The beam release vector was perpendicular to the ambient magnetic field direction, as was the separation vector between the release point and the PDP payload. The spin axis of the PDP payload was oriented to within 10 deg of this separation vector. At the moment of the first release, near apogee, the velocity of the payload ensemble was essentially perpendicular to both the ETG1 release vector and the PDP spin axis.

For the PDP on the APEX experiment, scientists at the Goddard Space Flight Center (GSFC) provided a variety of plasma instruments, as shown in Fig. 1. These included a three-axis double probe instrument for measuring dc and wave vector electric fields, a three-axis fluxgate magnetometer, and a Langmuir probe. The double probe consisted of booms that extended spherical probes with embedded preamps. As shown in Fig. 1, the two orthogonal, spin plane booms comprised 6.0-m tip-to-tip double probes between spheres 1 and 2 and between spheres 3 and 4. The spin-axis double probe (between spheres 1 and 5) was 1.0 m (tip to tip) and was directed toward the release. The Langmuir probe consisted of a 2.5-cm-diam spherical sensor with a titanium nitride surface that was situated 3 m from the main payload body. The Langmuir probe was operated in a swept configuration in order to measure absolute plasma density and temperature of the ambient plasma and was switched to a fixed-bias mode to measure relative ion plasma density and fluctuations during each release interval.

The GSFC instruments included a central electronics package that contained digital circuitry to acquire accurate measurements (e.g., 16-bit A/D conversions) with high temporal response, burst memories to gather large quantities of high-frequency data associated with the extremely short time duration releases, and electronics to perform onboard fast-Fourier-transform processing. The burst memory enabled three orthogonal very low-frequency (VLF) electric field

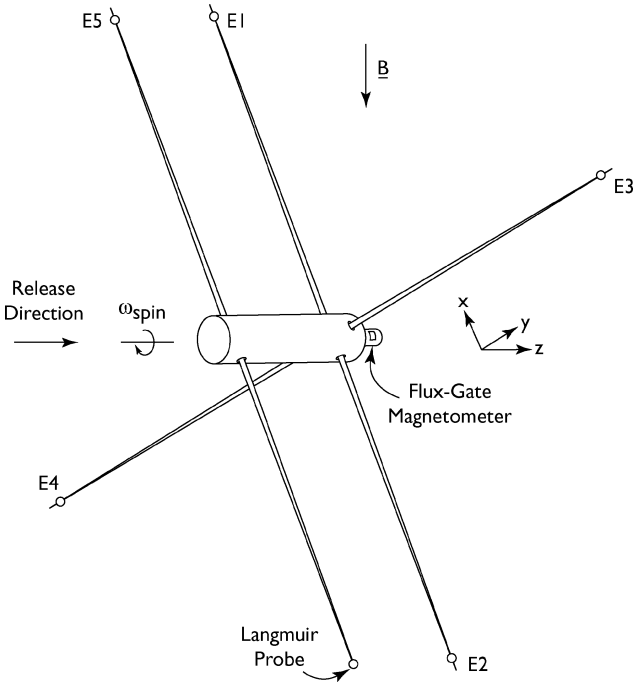

Fig. 1 Plasma diagnostic payload in the APEX experiment showing the location of the GSFC instruments and measurement geometry.

wave channels to be sampled at 128,000 s/s at 16 bit/channel for 5 s starting ~1 s prior to each release and one high-frequency (HF) electric field wave channel (along the release direction) to be sampled at 5 megasample at 12 bit/sample for 5 s, starting ~1 s prior to each release. The burst initiation also configured the Langmuir probe in its fixed-bias mode and reset the automatic gain control of a separate VLF electric field channel.

Data Presentation

In this section, we present an overview of the plasma density, magnetic field, and electric field measurements gathered on the PDP payload during the first release in the APEX experiment.

Plasma Density Data

The plasma density data are shown in the lowest panel of Fig. 2. This presentation includes composite data from both the low- and high-gain channels from the GSFC Langmuir probe as well as data from the Institute of Geospheres Dynamics Langmuir probe whose dynamic range was set to measure the very highest densities (see also Fig. 5 of Gavrilov et al.[8]).

The plasma density data reveal a well-defined, highly contained plasma perturbation with an extremely high number density, peaking at $4 \times 10^9/\text{cm}^{-3}$. This is the plasma density associated with the dense ion beam that is the subject of this paper. Notice that the leading edge (near 15 ms after the release time) is steeper than the trailing edge, implying that the beam is highly confined in velocity space on the leading edge, whereas it is spread out and/or contains slower-moving plasma on the trailing edge. Notice also the large-scale structure within the beam starting at about 8 ms after the release time. The data also reveal a well-defined spike at 345.14 s that likely corresponds to the response of the probe to ultraviolet and/or other intense electromagnetic radiation emitted at the precise time of the release.

Magnetic Field Data

The magnetic field data from the PDP payload are also shown in Fig. 2. The second panel from the bottom shows the total magnetic field intensity and illustrates the well-defined diamagnetic cavity associated with the high-density plasma beam. Notice that the absolute magnitude decreased to a value of ~7% of the ambient value (shown by the dotted line) in the center of the cavity.

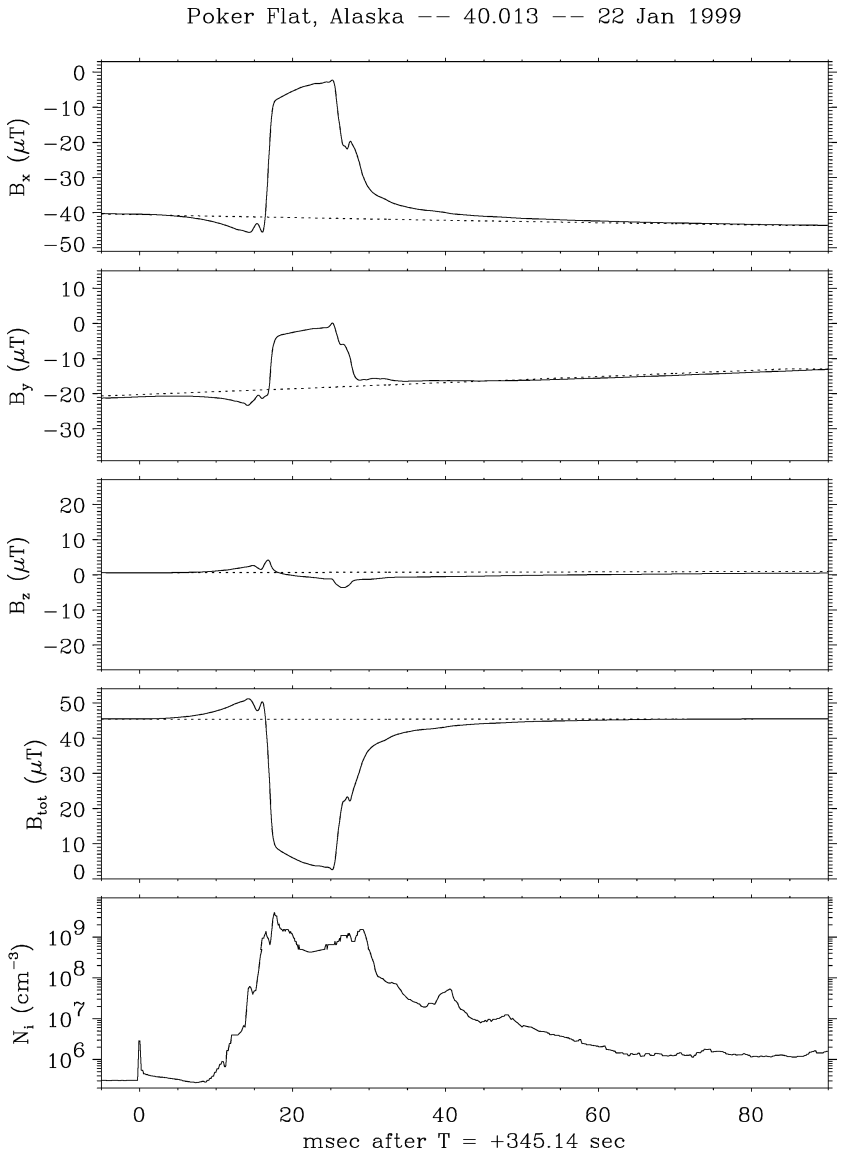

Fig. 2 Ion density and magnetometer data gathered on the PDP payload for the first APEX release.

The three magnetic field components, in the rocket reference frame, are shown in the top three panels. As shown in Fig. 1, the X and Y components are in the spin plane, whereas the Z component is along the payload spin axis, which corresponds approximately to the direction of the release vector. The dotted lines show the ambient levels, if there were no perturbation. Because the spin axis was oriented nearly perpendicular to the ambient magnetic field, the B_z background level is near zero. The slowly varying slope of the dotted lines in the B_x and B_y components are short segments of sinusoidal variations caused by the spin of the rocket. Notice that all three components show smooth deviations from their background levels that start at the release time of 345.14 s. As discussed later, we interpret these small ΔB variations as caused by a magnetosonic wave launched at the time of the release and propagating ahead of the plasma density wall. Other variations in the magnetic field data, observed in particular at either side of the diamagnetic cavity, were presumably caused by currents and Alfvénic perturbations.

To better characterize the magnetic perturbations, we now rotate these fields from the rocket coordinate system to a magnetic coordinate system shown in Fig. 3. Here, we define $B_\parallel$ as the direction along the ambient magnetic field direction. We define two components perpendicular to this direction: $B_{\perp 1}$ is perpendicular to $B_\parallel$ and is approximately within the rocket spin plane, while $B_{\perp 2}$ is perpendicular to $B_\parallel$ and is approximated along the spin axis. Note that the release velocity was along $B_{\perp 2}$ to within 10 deg.

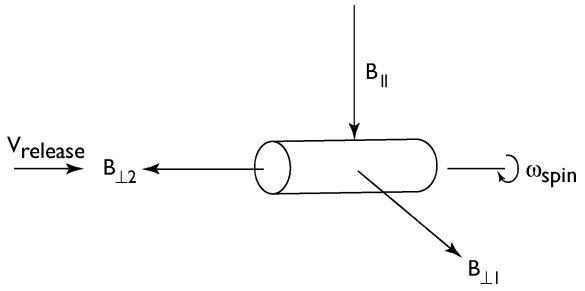

Fig. 3 Coordinate system composed of the component along the ambient magnetic field direction and two perpendicular components along, and perpendicular to, the release direction.

The magnetic field data from Fig. 2 are now rotated to this new coordinate system in Fig. 4, in which we present the variations of the magnetic field in each direction defined in Fig. 3. The top panel shows the component along the magnetic field direction. This includes both the very strong depletion of $\sim 42\mu$T as a result of the diamagnetic cavity as well as the gradual rise in ΔB that started at the release time and is attributed to a magnetosonic wave.

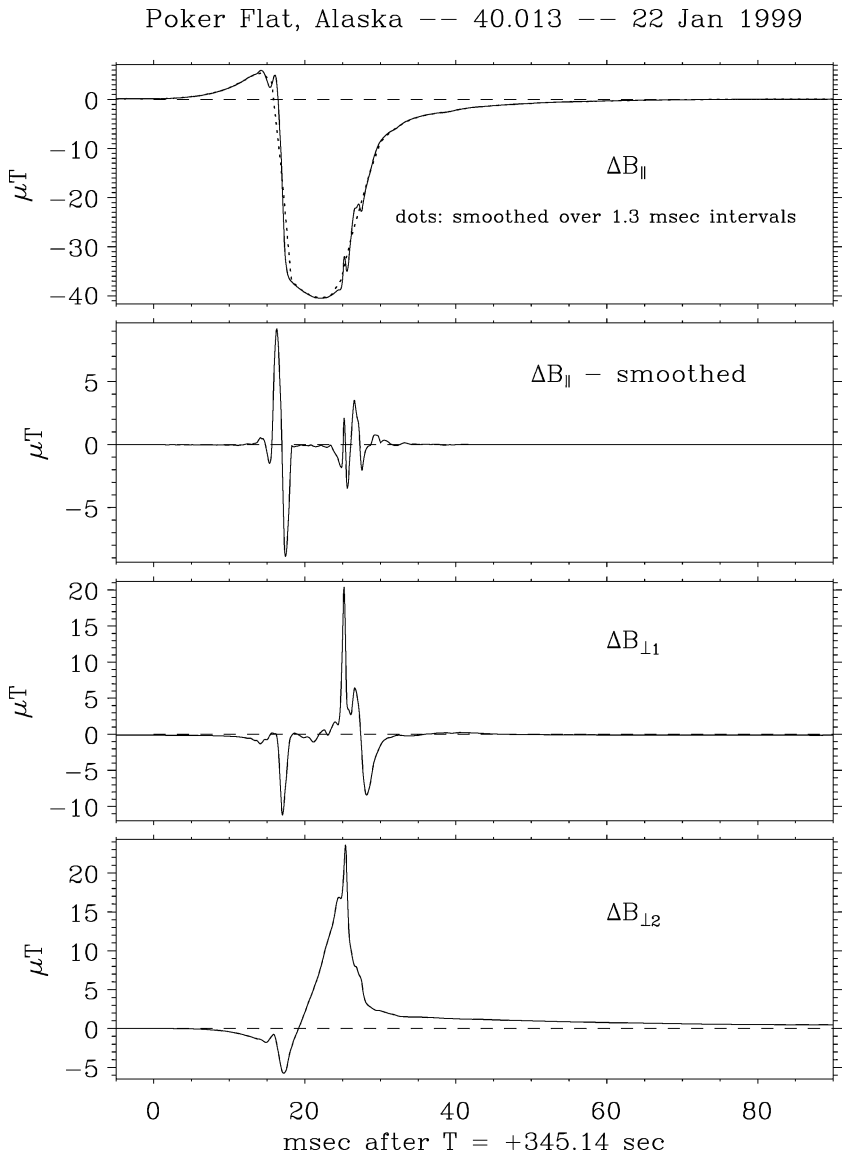

Fig. 4 Magnetic field data rotated to the coordinate system shown in Fig. 3.

The $\Delta B_{\parallel}$ component includes smaller-scale variations near the edges of the diamagnetic cavity. To better evaluate these small variations, we have smoothed the data by computing an average over 1.31-ms bins. The smoothed data are shown by the dotted line in the same panel. The difference between the high-resolution data and the averaged, smoothed $\Delta B_{\parallel}$ waveforms is shown in the second panel. Notice the large variations at the leading and trailing edges of the diamagnetic cavity. We attribute these to the large diamagnetic currents that surround the cavity in a belt configuration in the plane perpendicular to the magnetic field. The bipolar signature implies that the diamagnetic cavity is accompanied on each side by a ΔB (and hence, a current) of opposite sense.

The lowest two panels in Fig. 4 show the ΔB signatures perpendicular to the ambient magnetic field direction. These also show strong signatures that indicate the presence of parallel or field-aligned currents.

The interpretation of the ΔB signatures in terms of conduction currents (i.e., $\nabla \times \boldsymbol{B} = \boldsymbol{J}$) is not straightforward because the geometry of the ion beam cannot be represented by that of infinite slabs of current. Such assumptions are typically invoked in space physics research to interpret magnetic field variations in terms of conduction currents. Although the geometry is less certain in this experiment, the ΔB signatures are highly suggestive that both strong perpendicular and parallel conduction currents are present and that they are strongest at the sides of the diamagnetic cavity. Furthermore, we note that the plasma density itself was modulated, as shown in Fig. 2. This modulation would also produce variations in the conduction current and hence in magnetic field signatures in a probe across which such a current ensemble were to pass. Our next step is to investigate the electric fields associated with the high-density beam and the subsequent $\boldsymbol{E} \times \boldsymbol{B}$ motions of the plasma.

DC Electric Field Data

The dc electric field data are shown in Fig. 5. In the lowest two panels, the density data and the total magnetic field intensity from Fig. 2 are repeated for reference. The third panel from the bottom shows the total dc electric field. Notice that the total field increases in a smooth and continuous fashion to about 0.5 V/m for the first 10 ms after the release. The field then continues to increase to 1.5 V/m in the next 8 ms, although it now contains considerable structuring during this latter interval. We interpret this structure as that caused by large-scale, electrostatic irregularities and Alfvénic perturbations that appear to be superimposed on the increasing dc electric field level. After the dc electric field reaches a peak magnitude of 1.5 V/m, it then diminishes quickly to a value near zero within the diamagnetic cavity. The electric field returns to a value near 1 V/m on the trailing edge of the cavity.

The three electric field components in the rocket reference frame are shown in the upper three panels. The E_x and E_y data are in

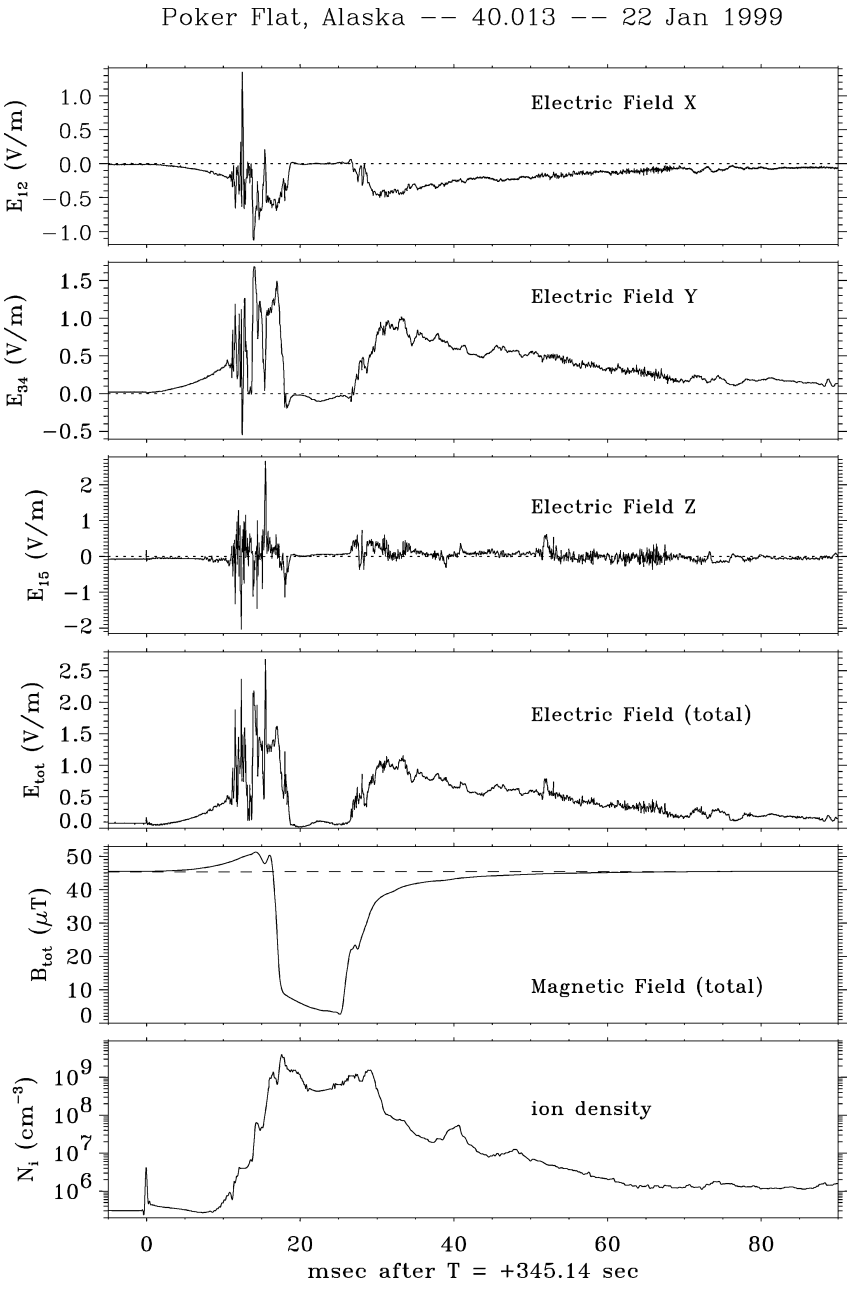

Fig. 5 DC electric field data gathered on the PDP payload during the first release, with the plasma density and total magnetic field data included for reference.

the spin plane and correspond to the field components measured by double probes consisting of sphere pair 1 and 2 and sphere pair 3 and 4, respectively. These components are parallel to the respective B_x and B_y magnetic field components shown in Fig. 2. The E_z data are along the spin axis (parallel to the B_z magnetic field component shown in Fig. 2) and correspond to the electric fields measured by the double probe consisting of sphere pair 1 and 5. This component is approximately in the direction of the release vector.

Notice that the dc electric field components in the spin plane increase prior to the magnetic cavity and contain large variations on either side of the cavity that likely correspond to Alfvénic perturbations and other waves surrounding the release. The smooth increase beginning at the release time of 345.14 likely corresponds to a fast magnetosonic wave, discussed later. The small pulse in the electric field data of 345.14 corresponds to the initial release time also identified in the Langmuir-probe data shown in Fig. 2. The $\boldsymbol{V} \times \boldsymbol{B}$ electric field caused by the motion of the payload across the magnetic field has not been removed. During the first release that concerns us here, this contribution corresponded to a field of 78 mV/m that was primarily in the spin-axis (E_z) direction.

Our next task is to rotate the electric field data from payload coordinates into a more meaningful coordinate system. We use the measured magnetometer data to calculate the two components of the electric field perpendicular to the magnetic field as well as the electric field component parallel to the magnetic field, using the same coordinate system shown in Fig. 3. These electric field components and their associated $\boldsymbol{E} \times \boldsymbol{B}$ velocities are shown in Fig. 6.

Notice immediately the parallel electric field component in the top panel that takes the form of a bipolar structure at the inner edges of the diamagnetic cavity. This is particularly pronounced on the leading edge of the cavity at ~18 ms after the release. Higher-frequency parallel electric field components are also present, particularly on the leading edge of the ion beam. The dc parallel electric fields are part of the electrodynamic response to the high-velocity, overdense ion beam that is set up to help ensure current continuity within and around the highly localized diamagnetic cavity.

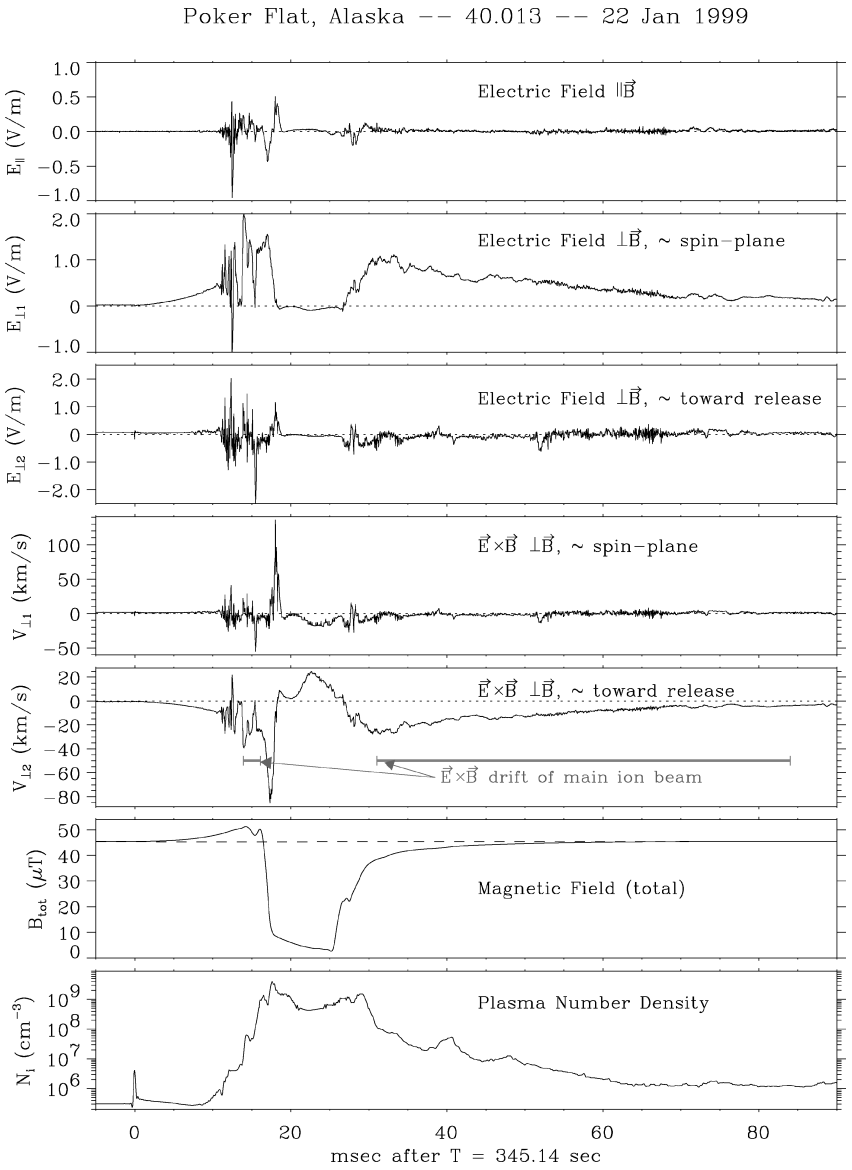

Fig. 6 Electric field data (top three panels) rotated to the coordinate system shown in Fig. 3. The next two panels show the $E \times B$ velocity components in this same coordinate system, followed by the density and magnetic data for reference.

The next two panels in Fig. 6 show the perpendicular electric field components. Notice that the dc electric field component consists of a large-amplitude, slowly varying component that is primarily in the $E_{\perp 1}$ direction, that is, both perpendicular to the magnetic field and to the release vector. This $E_{\perp 1}$ field constitutes both the main contribution to the $\boldsymbol{E} \times \boldsymbol{B}$ plasma velocity associated with high-density beam and also the ΔE component of a magnetosonic wave propagating immediately ahead of the beam.

The $\boldsymbol{E} \times \boldsymbol{B}$ velocities are shown in the next two panels, in which most of the velocity is in the component $V_{\perp 2}$ that contains the release direction. Notice the ~25 km/s $\boldsymbol{E} \times \boldsymbol{B}$ velocity away from the release (i.e., $-V_{\perp 2}$ component) associated with the leading edge of the high density beam near 14–16 ms after the release and just prior to the magnetic cavity. This velocity corresponds to the bulk speed of the ion beam. As discussed next, on the trailing edge of the magnetic cavity the main $\boldsymbol{E} \times \boldsymbol{B}$ velocity is also ~25 km/s away from the release, tapering down after this as the slower plasma arrives at the payload. The $\boldsymbol{E} \times \boldsymbol{B}$ velocity measurements on the inner edges of the diamagnetic cavity and within the cavity are difficult to interpret as the magnetic field changes so abruptly, with timescales much faster than that of an aluminum ion gyro period. Thus, we do not interpret the −80-km/s velocity calculation (near 17 ms after the release), or those velocity calculations within the diamagnetic cavity, as true $\boldsymbol{E} \times \boldsymbol{B}$ velocities associated with the proper ion motion. We return to this point in the discussion section.

The electric field data prior to the arrival of the bulk ion beam cannot be interpreted as that associated with the ion beam $\boldsymbol{E} \times \boldsymbol{B}$ velocity because the ion beam has not yet arrived. Rather, we interpret the slow increase in both ΔE and ΔB as being caused by a magnetosonic wave. The resulting $\Delta \boldsymbol{E} \times \Delta \boldsymbol{B}$ velocities are shown in Fig. 7. These velocities have been calculated from the three ΔB components in Fig. 4 and the three ΔE components using the data in Fig. 6 in which the relatively small ambient electric field have been subtracted. Because the main contributions are from $\Delta E_{\perp 1}$ and $\Delta B_{\parallel}$, we show those components in Fig. 7 for reference. Notice that the main $\Delta \boldsymbol{E} \times \Delta \boldsymbol{B}$ velocity prior to the arrival of the main ion beam is away from the release in the $\Delta V_{\perp 2}$ direction. After the initial startup, the total perpendicular velocity shows a fairly constant velocity at approximately 160 km/s.

Figure 7 also includes a panel (at the bottom) showing the $\boldsymbol{E} \times \boldsymbol{B}$ component of $V_{\perp 2}$ from Fig. 6 for comparison of the two sets of calculated velocities. This comparison demonstrates how the measured ΔE component includes contributions from the magnetosonic wave at the start of the release as well as from the electric field associated with the main ion beam that follows the magnetosonic wave. We return to this dichotomy in the Discussion section.

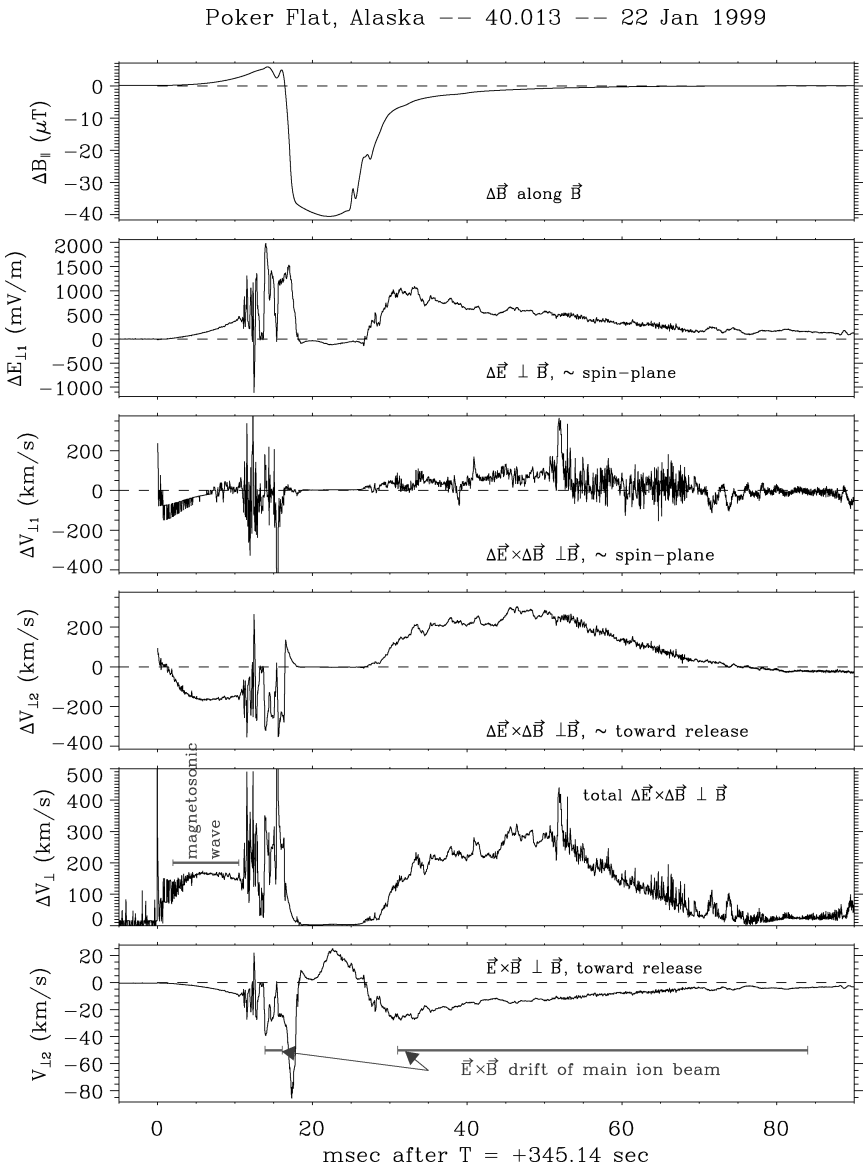

Fig. 7 Wave magnetic and electric field data and their associated $\Delta E \times \Delta B$ velocities. The $E \times B$ component along $V_{\perp 2}$ is shown for reference.

VLF Electric Field Wave Data

Time series of the electric field wave data from the VLF burst channels are shown in Fig. 8a for 0.52 s of the burst. The VLF wave electric field data were passed through an onboard bandpass filter between 50 Hz and 64 kHz (3-dB frequencies) with a gain factor that has been accounted for in this presentation. The data were sampled at 128 ksamples/s for each channel.

The VLF electric field data reveal a complex set of waves associated with the release. Although the data are saturated during portions of the time corresponding to the main ion beam perturbation, they nevertheless reveal a large-amplitude envelope with a period near 20 ms that dominates for a few cycles within the main ion beam and appears to be "controlled" by the width of the diamagnetic cavity. This waveform is particularly prominent in the δE_x (VLF12) and δE_y (VLF34) data, which are perpendicular to the release direction. These are followed by spikey electric fields in all three components.

An enlargement of these data corresponding to 16 ms associated with the initial release time is shown in Fig. 8b. This high-resolution data presentation reveals both a bipolar release spike, as well as precursor waves near the ambient lower hybrid frequency. Notice that the release spike and subsequent wave activity are largest in the δE_z (VLF15) component that corresponds to the direction of the release velocity.

A spectrogram of the δE_z wave electric field component (VLF15) along the release direction is shown in the second panel from the top of Fig. 9. The spectrogram was computed using Hanning windows and a 50% overlap between successive Fourier transforms. Notice the very strong waves surrounding the diamagnetic cavity region with increased wave activity in the trailing portion. Coincident with the spike corresponding to the release initiation, waves near 7 kHz that correspond to the ambient (O^+) lower hybrid frequency appeared. It is difficult to discern the emissions at the lower hybrid frequency in the spectrogram in Fig. 9 because the time duration of the event was very limited. However, these waves are very clearly shown in the time-series data in Fig. 8b.

HF Electric Field Wave Data

A high-frequency spectrogram from the HF15 burst channel is shown in the top panel of Fig. 9. These data are from the axis along the payload (i.e., along the release vector), which were passed through a bandpass filter between 3 kHz and 2.5 MHz (3-dB frequencies). The data reveal a complicated high-frequency wave structure. The spike at 345.14 s corresponds to the electric field perturbation at the release time just noted. Note the high-frequency whistler-like waves after the release and prior to the onset of lower-frequency waves. These were almost certainly launched by the electromagnetic

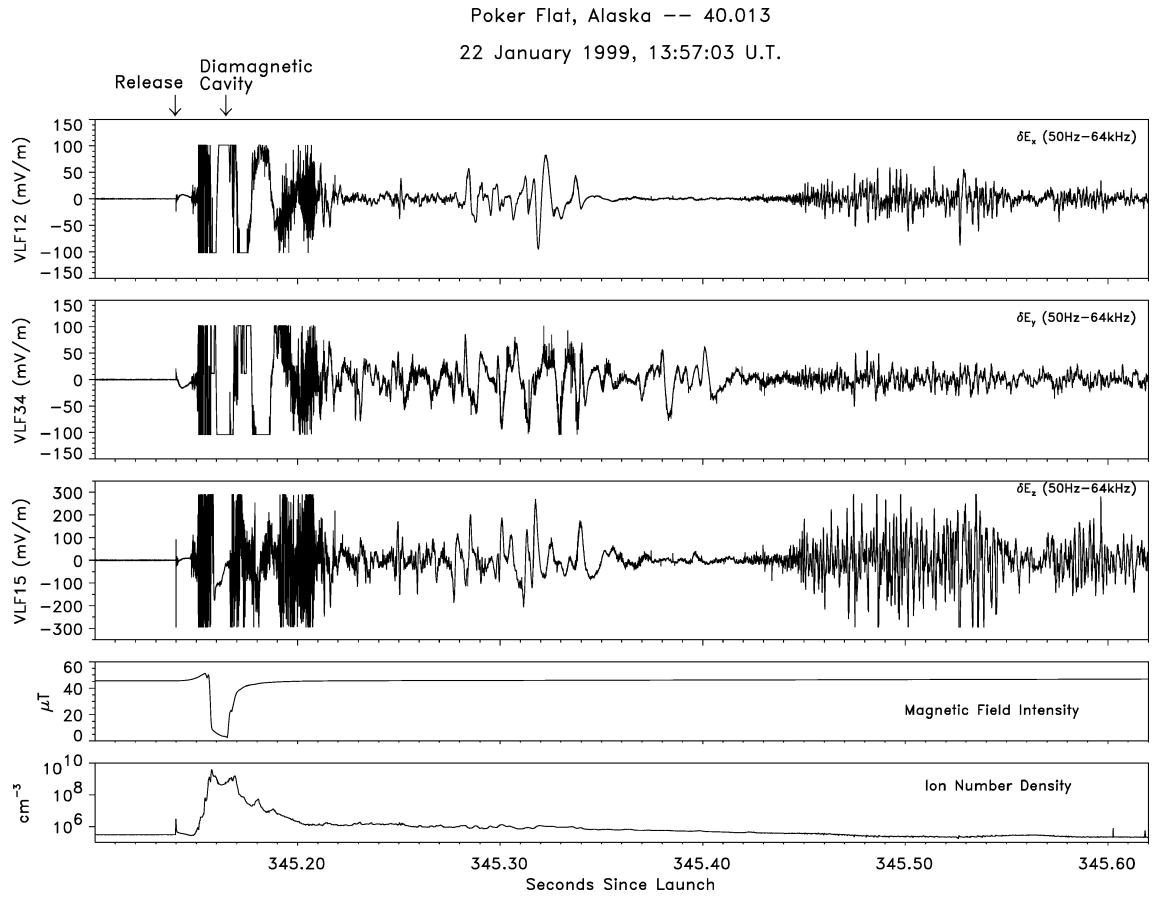

Fig. 8a VLF electric field data for all three components during the release. Note the change in scale for the δE_z component. The magnetic field and plasma density data are included for reference.

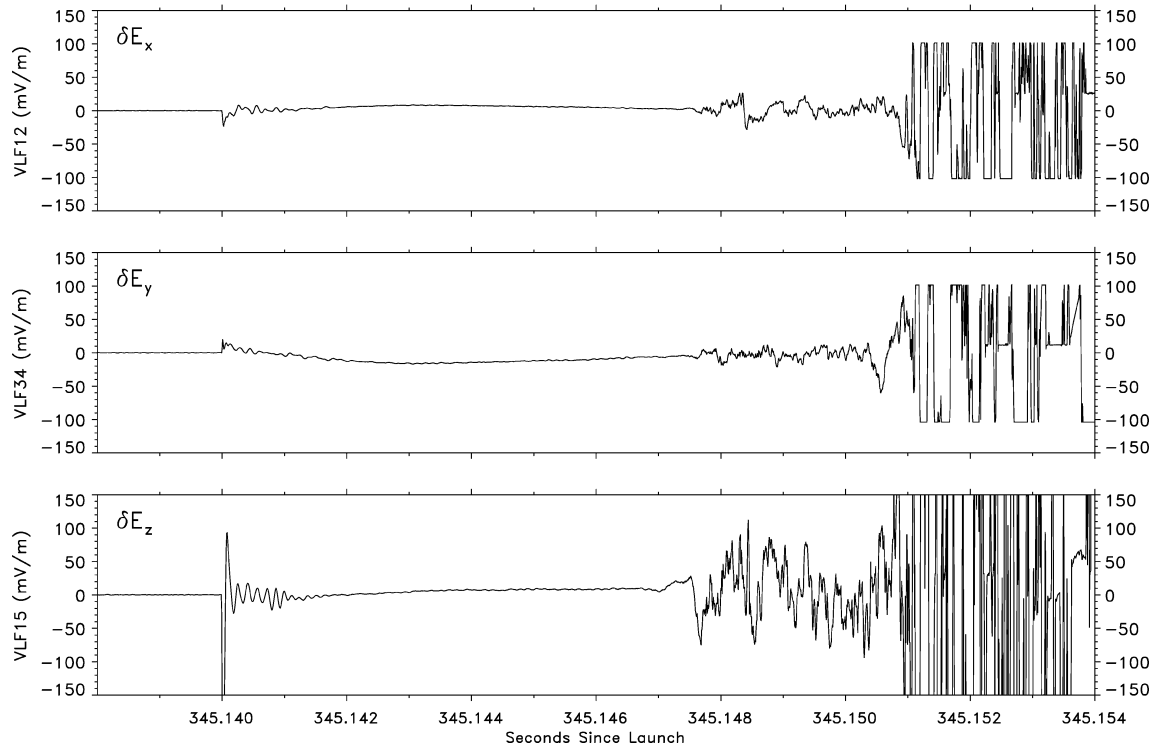

Fig. 8b Expanded view of the data in Fig. 8a revealing the detailed waveforms associated with the release time, as well as precursor waves prior to the arrival of the bulk ion density.

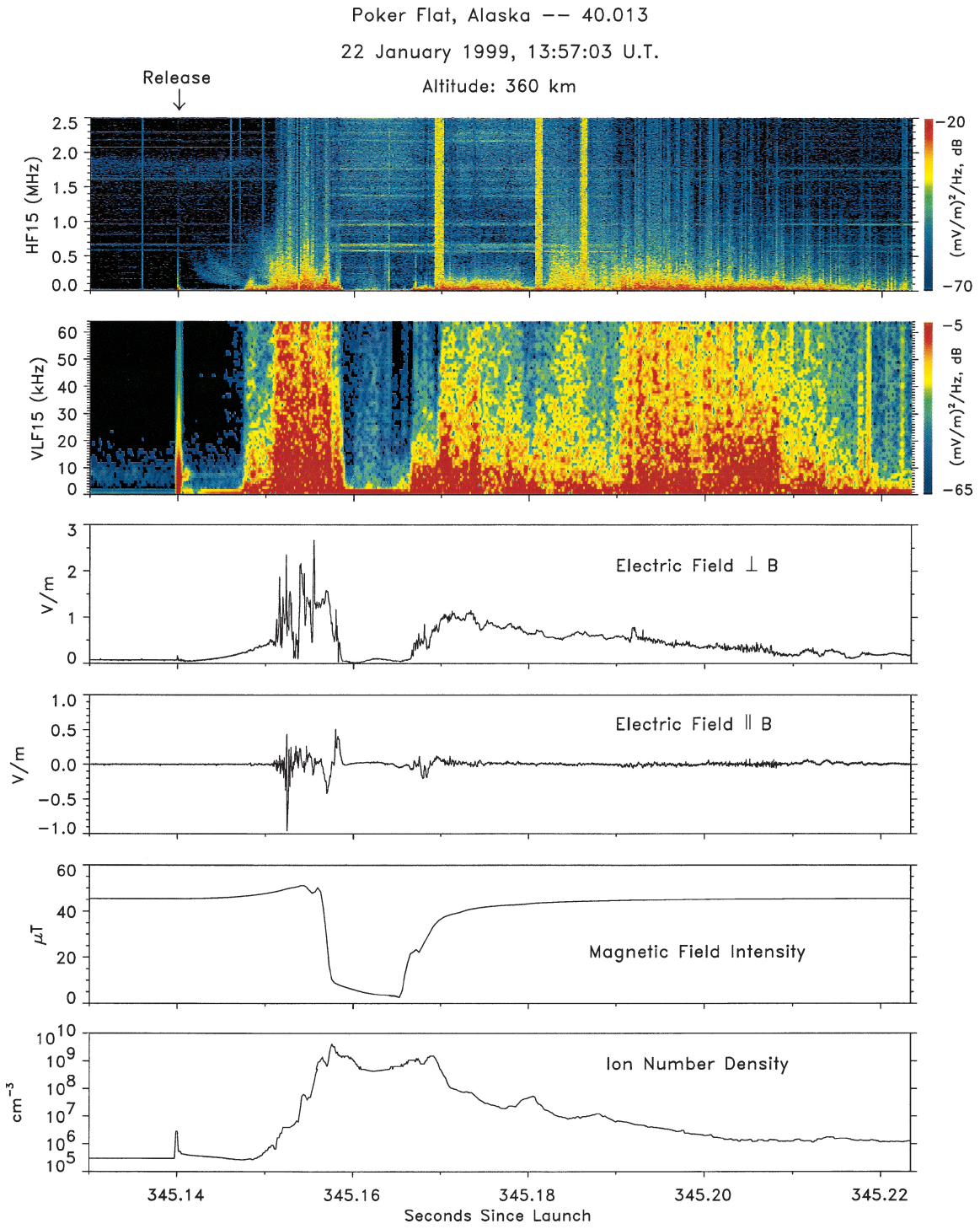

Fig. 9 Composite of the ion density data, magnetic field magnitude, perpendicular and parallel dc electric field components, and VLF and HF spectrograms corresponding to the electric field wave component along the release direction δE_z.

pulse associated with the release. Notice the strong lower frequency irregularities and turbulence associated with the beam on each side of the diamagnetic cavity that are also present during the extended trailing edge of the beam. Although the strongest amplitudes are below a few 100 kHz, notice that in some cases the wave spectra extend beyond 1 MHz.

In this presentation, the discrete horizontal banding, for example near 650 and 950 kHz within the diamagnetic cavity, is caused by payload interference, which varies in intensity as a function of the ambient plasma density, becoming more significant inside the beam where the ion density was quite high. The vertical bands near 345.17, 345.18, and 345.185 s are a result of telemetry dropouts that occurred during the transmission of the burst data to the ground during the 3 min of flight time after the release that were used to transmit these data to the ground.

Ensemble Data Presentation

The dc electric field, dc magnetic field, and plasma density are also included in Fig. 9 for direct comparisons with the wave data. Notice the relative location of the dc and wave electric field signatures associated with the dense plasma beam but are clearly modulated by the

diamagnetic cavity evident in the magnetic field data. Specifically, notice that both the VLF and HF waves are enhanced on the sides of the diamagnetic cavity, but are considerably diminished within the cavity itself. We now discuss the main features of the observations presented here and their interdependency with each other.

Discussion

The data presented here reveal a complex electrodynamic structure associated with a diamagnetic cavity created by an overdense, high-velocity aluminum ion beam released in the earth's ionosphere. Figure 10 provides a sketch illustrating some of the observed electrodynamic features associated with the diamagnetic cavity. The strong dc electric fields perpendicular to the release velocity vector, the high-density ion beam, and the magnetic cavity correspond to the direct measurements presented here. Other features of the data, such as the parallel electric field bipolar layer, inferred field-aligned and diamagnetic currents, and inferred Alfvén waves on either side of the cavity are also indicated in the sketch. The large perpendicular electric field $E_\perp$ is separated into dashed and solid lines to indicate the fact that it represents first a magnetosonic wave and then that corresponding to the $\boldsymbol{E} \times \boldsymbol{B}$ velocity of the ion beam itself. Below, we discuss these features associated with the ion beam and diamagnetic cavity in more detail.

Overdense Ion Beam

The experiment described here is that of an overdense, highly contained, aluminum ion beam released in an ambient, O^+ plasma such that

$$n_{\text{beam}} \gg n_{\text{ionosphere}}$$

Peaking at 4×10^9 ions/cc, the beam density is about 10^4 times that of the background ionosphere. The plasma frequency associated with this density is 570 MHz, well above the upper frequency response of the electric field instrument used in this experiment. The large plasma density is similar to that reported in previous experiments using this type of explosive generation[8] and can include contributions from the critical velocity effect.[9] Although the beam has been very efficiently ionized, because of recombinations it includes some fraction of neutral aluminum atoms when it reaches the PDP payload.

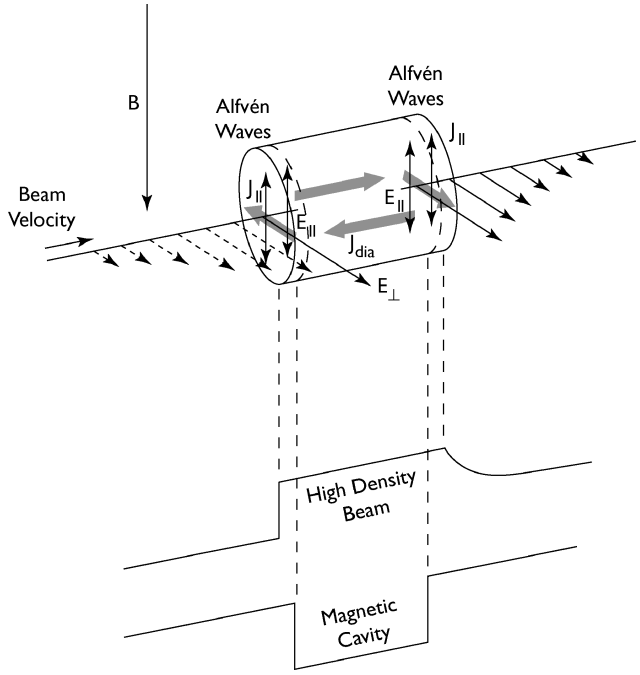

Fig. 10 Sketch illustrating the main electrodynamics features of the first APEX release as suggested by the data gathered by instruments on the PDP payload presented here.

Beam Velocity

The positions of the release module and PDP payloads are known with a high degree of accuracy from their onboard global-positioning-system measurements. The relative spacing between these two platforms was 468 m at the time of the release. The main wall of high density ions arrived 14 ms later, corresponding to a mean velocity of 33–34 km/s. The fastest particles appeared to arrive after only 8 ms, corresponding to a velocity of 58.5 km/s. Such fast particles can include those associated with energetic ambient O^+ ions accelerated by collisions with the aluminum atoms. We return to these velocities below when we compare them to the measured $\boldsymbol{E} \times \boldsymbol{B}$ velocities.

Beam Dimensions

The physical size of the main beam is seen to be only 670 m in length along the measurement vector, based on the mean bulk velocity discussed immediately above and the fact that the main beam lasted for ~20 ms in the data. Optical measurements[1] have also demonstrated that the main beam is very narrow (~10-deg half-width). Assuming the perpendicular ion velocity can be considered that of its initial release speed of 33.5 km/s, the Larmor radius of an Al^+ ion is about 200 m, or half this value for an Al^{++} ion. Thus, the ion beam dimension is on the order of a few ion Larmor radii.

Diamagnetic Cavity

The central electrodynamic feature associated with the high-density ion beam is the diamagnetic cavity observed in the magnetic field data. Indeed, as shown in Fig. 2, the magnetic intensity in the center of the cavity decreased to a value of approximately 7.5% of the total background field.

The diamagnetic cavity is formed when the particle pressure exceeds that of the magnetic pressure. We equate the particle pressure of the plasma beam with that of the perturbed magnetic field pressure in the observed diamagnetic cavity to determine whether the observed cavity represents both a reasonable and fully developed manifestation of the overdense plasma beam in the Earth's magnetic field. Essentially, we have

$$\Delta N K_B T = (\Delta B)^2 \big/ 2\mu_0$$

It is not clear what value to use for the temperature of the bulk plasma beam. If we assume the temperature is 1 eV (or 11,600 deg), for a beam density of 4×10^9 cm^{-3} the first term equals 1.6×10^{-4} Pa. Similarly, a magnetic field perturbation of 42 μT provides a magnetic pressure of 7.0×10^{-4} Pa. The two pressures are quite similar. Variations in the temperature is one source for the discrepancy, and indeed a temperature of 4.38 eV would make the two pressures equal. Note also that the payload might not have been situated in the exact center of the cavity, although we believe it is probably not far off. Computer simulations also reproduce a diamagnetic cavity with similar characteristics, as shown within Delamere et al.[10] and Gastonis et al.[11]

Plasma Velocities

The $\boldsymbol{E} \times \boldsymbol{B}$ plasma velocities associated with the ion beam can be determined by the dc electric field measurements perpendicular to the magnetic field. In Fig. 6, the gray bars indicate where the beam density is large, yet the effects of the large-scale irregularities and diamagnetic cavity are not pronounced. The $\boldsymbol{E} \times \boldsymbol{B}$ velocity within the leading edge of the beam is ~25 km/s directed away from the release point. This is similar to the measured $\boldsymbol{E} \times \boldsymbol{B}$ velocity on the trailing edge of the cavity, which then tapers off in concert with the diminishing ion beam density. The 25-km/s velocity is less than the 33.5-km/s velocity estimated from the arrival time of the beam and indicates that the beam is braking. The electric and magnetic signatures can also include contributions from magnetosonic waves as discussed next.

Notice that at the inner edge of the cavity the computed $\boldsymbol{E} \times \boldsymbol{B}$ velocity away from the release is quite high (~80 km/s) and certainly

is not realistic. This value results from the fact that the magnetic field is decreasing very rapidly in a confined region much smaller than the ion gyro radius and within a time period much smaller than the ion gyro period.

Inside the diamagnetic cavity (e.g., from ~18–27 ms after the release), the perpendicular dc electric field reverses sign, implying at first glance that the plasma velocity reverses direction. However, from simple momentum arguments we know the beam continued along its proper direction. The reverse electric field in the cavity can be caused by a superimposed polarization field associated with the braking that is not evident where the dc electric field is large (~1 V/m) yet becomes apparent in the cavity where the electric field associated with the ion plasma drift is considerably smaller because the magnetic field here is smaller. Furthermore, because the magnetic field in the cavity becomes considerably smaller the local ion gyro period and radius both become large compared to the diamagnetic cavity time and distance scales and hence the $\boldsymbol{E} \times \boldsymbol{B}$ drift calculations here become even more difficult to interpret.

Parallel Electric Fields

Associated with the complex electrodynamics and braking of the ion beam is the creation of parallel electric fields and field-aligned currents. The clearest evidence for this is the bipolar parallel electric field at the leading edge of the cavity. There is also evidence for such a signature on the inner, trailing edge of the cavity, although it is not as distinct. The creation of localized parallel electric fields is not unlike the situation in the aurora where parallel electric fields are set up to ensure current continuity when dense, energetic plasma beams are injected into colder plasma regions along converging magnetic field lines. In our case, the plasma beam is also highly confined, and a diamagnetic cavity is formed by its very large plasma number density. Given the high velocity of the release, the data suggest that intense currents associated with the diamagnetic cavity and with the coupling to the ambient plasma result in the formation of current driven instabilities and parallel electric fields.

Alfvén Waves and Magnetosonic Waves

Large-amplitude, wave-like, low-frequency ($< \sim$ 1-kHz) structures were observed on both sides of the diamagnetic cavity although predominantly on the leading edge. These waves have amplitudes on the order of ± 1 V/m including significant components along the magnetic field direction. We believe these wave structures are Alfvénic and likely transfer momentum to the background plasma and further slow the ion beam.[3]

Magnetosonic waves were observed at the very onset of the release, prior to the arrival of the bulk ion beam. Beginning ~1 ms after the release time, these waves were detected in both a ΔB (mostly along B) waveform and a ΔE waveform (mostly perpendicular to both B and to the release direction) before the arrival of the fastest ion beam particles. Because these waves appeared just after the time of the release but clearly ahead of the fastest ion beam particles, we associate them with an electromagnetic wave traveling near the local Alfvén speed. The measured $\Delta E/\Delta B$ velocity of this wave is approximately 160 km/s. For reference, the Alfvén speed that would correspond to the ambient O^+ plasma density of $2 \times 10^5/\text{cm}^3$ is 550 km/s.

There is some overlap between the signatures that we associate with the magnetosonic wave and those associated with the $\boldsymbol{E} \times \boldsymbol{B}$ motion of the plasma, local currents, and Alfvén wave perturbations, as shown in Fig. 7. In particular, notice that the smoothly increasing ΔB signature continues until it encounters larger perturbations caused by currents just at the edge of the diamagnetic cavity. The smoothly increasing ΔE signature is interrupted by abrupt electric field perturbations, presumably because of electrostatic irregularities and other waves. The dc electric field after that (and prior to the diamagnetic cavity) appears to be associated with the $\boldsymbol{E} \times \boldsymbol{B}$ plasma drift of the main ion beam, consistent with the $\boldsymbol{E} \times \boldsymbol{B}$ velocity (~25 km/s) observed just after the diamagnetic cavity. How the combined contributions of the many plasma processes are manifest in the electric field and magnetic field data is considerably complex and requires further analysis.

Other Plasma Waves

Several other plasma waves were associated with the release and observed in this experiment. We comment briefly on these next.

Intense plasma turbulence with amplitudes of several hundred millivolts/meter and greater and frequencies extending to >1 MHz in the payload reference frame were observed on each side of the cavity. These waves are believed to travel with the ion beam/diamagnetic cavity ensemble and might be responsible for plasma heating and possibly plasma generation via a critical velocity effect.[4,9]

Narrow bandwidth waves associated with the lower hybrid frequency of the ambient O^+ ionosphere plasma were observed at the onset of the release. These waves appear to be whistler-mode electromagnetic waves, possibly associated with accelerated electrons at the release point, in a similar manner to the generation of VLF auroral hiss. Incidentally, this frequency of about 7 kHz corresponds to the lower cutoff of the natural VLF auroral hiss observed prior to the release, which is known to occur at the lower hybrid frequency.

Electrostatic waves appearing after about 8 ms and coincident with the fastest particles (as seen in the Langmuir-probe data) might have been caused by a two-stream instability involving the ambient O^+ ions and either the fastest Al^+ ions and/or locally accelerated O^+ ions pushed ahead by the aluminum beam. These precursor waves also occur at the ambient O^+ lower hybrid frequency, although this frequency is less distinct in the wave data presented here.

The high-frequency wave data included a descending whistler-like frequency dispersion that was clearly associated with the electromagnetic pulse at the time of the release. These waves resemble medium frequency whistlers reported by Kelley et al.[12] associated with lightning bursts in the ionosphere.

Trailing the cavity are a variety of lower-frequency wave modes with strong electric field amplitudes (>100 mV/m). These waves appear to be ion acoustic turbulence, suggesting $T_e > T_i$. They are not unlike waves reported in the trailing debris clouds of ion releases detected in other experiments conducted in the ionosphere.[13,14]

Conclusions

The Active Plasma Experiment (APEX) measurements reveal a complex electrodynamics associated with a high-velocity aluminum ion release. The following characteristics summarize the most important observations:

1) A narrowly confined, overdense ion beam of over 10^9 cm^{-3} was released in the Earth's ionosphere that traveled at a speed of near 33.5 km/s with spatial scales on the order of a few gyro radii at a distance of ~0.5 km away from the release point.

2) A well-defined, diamagnetic cavity with a 93% magnetic depletion within a spatial scale of ~500 m was observed associated with the high-density plasma pulse or beam. The observed diamagnetic cavity is consistent with the calculated particle pressure of the ion beam.

3) The dc electric field increased to values of ~1.5 V/m at the leading edge and at 1.0 V/m at the trailing edges of the diamagnetic cavity, yet decreased to about 0.1 V/m inside the diamagnetic cavity.

4) The main $\boldsymbol{E} \times \boldsymbol{B}$ plasma velocity was ~25 km/s away from the release point, as measured by the dc electric field, both prior to and immediately following the diamagnetic cavity.

5) The smoothly increasing ΔE and ΔB signatures prior to the arrival of the fastest particles correspond to a magnetosonic wave launched ahead of the beam traveling at a speed near 160 km/s as measured by $\Delta E/\Delta B$.

6) Variations in the magnetic field data provide evidence for currents on the sides of the density pulse, including field-aligned currents surrounding the leading and trailing edges of the diamagnetic cavity that presumably helped sustain the high-velocity plasma beam.

7) Bipolar, parallel electric fields exist at the sides of diamagnetic cavity, as well as with higher frequencies on the leading edge in this

region. Such fields can arise in order to maintain current continuity and can be expected to accelerate energetic particles in the vicinity of the ion beam boundaries.

8) Strong, broadband plasma irregularities extending to >1 MHz were observed on each side of the cavity and can be associated with mechanisms that produce significant plasma heating. The presence of such waves was markedly diminished within the cavity itself.

9) Plasma waves at the ambient O^+ lower hybrid frequency were observed coincident with the release time that were likely caused by electromagnetic waves possibly associated with electrons accelerated by the release.

10) A high-frequency whistler was observed associated with the electromagnetic pulse coincident with the release.

The APEX measurements provide a self-consistent picture of the plasma physics surrounding a high-velocity, overdense ion beam released in the high-latitude ionosphere. A large diamagnetic cavity was formed, with associated dc electric fields including parallel electric fields, Alfvénic perturbations, magnetosonic waves, and a variety of other plasma waves.

Because the experiment was conducted in space, there are no laboratory chamber walls to impede the evolution and nonlinear development of the plasma phenomena. The phenomena were observed with a nearly complete set of plasma diagnostics that enabled the measurement of the relevant plasma parameters with a high degree of confidence. This research furthers our understanding of high-speed, localized overdense ion beams in the space environment and their associated electrodynamics.

Acknowledgments

The Active Plasma Experiment (APEX) science team acknowledges the expert design, fabrication, test, and launch of the APEX plasma-diagnostics-payload payload by the NASA Wallops Flight Facility sounding rocket payload team, under the direction of Frank Lau, Payload Manager. We acknowledge Steve Martin's expert assistance with the data presentation.

References

[1]Erlandson, R. E., Meng, C. I., Swaminathan, P. K., Kumar, C. K., Dogra, V. K., Stoyanov, B. J., Gavrilov, B. G., Kiselev, Y., Zetzer, J. I., Stenbaek-Nielsen, H. C., Lynch, K. A., Pfaff, R. F., Delamere, P. A., Bounds, S., and Gatsonis, N. A., "North Star Plasma-Jet Space Experiment," *Journal of Spacecraft and Rockets*, Vol. 41, No. 4, 2004, pp. 483–489.

[2]Kelley, M. C., Swenson, C. M., Brenning, N., Baker, K., and Pfaff, R., "Electric and Magnetic Field Measurements Inside a High-Velocity Neutral Beam Undergoing Ionization," *Journal of Geophysical Research*, Vol. 96, No. A6, 1991, pp. 9703–9718.

[3]Brenning, N., Falthammar, C.-G., Haerendel, G., Kelley, M. C., Marklund, G., Pfaff, R., Providakes, J., Stenbaek-Nielsen, H. C., Swenson, C., Torbert, R., and Wescott, E. M., "Interpretation of the Electric Fields Measured in an Ionospheric Critical Ionization Velocity Experiment," *Journal of Geophysical Research*, Vol. 96, No. A6, 1991, pp. 9719–9733.

[4]Torbert, R. B., Kletzing, C. A., Liou, K., and Rau, D., "Prompt Ionization in the CRIT II Barium Releases," *Geophysical Research Letters*, Vol. 19, No. 10, 1992, pp. 973–976.

[5]Swenson, C. M., Kelley, M. C., Primdahl, F., and Baker, K. D., "CRIT II Electric, Magnetic, and Density Measurements Within an Ionizing Neutral Stream," *Geophysical Research Letters*, Vol. 17, No. 12, 1990, pp. 2337–2340.

[6]Kelley, M. C., Pfaff, R. F., and Haerendel, G., "Electric Field Measurements During the Condor Critical Velocity Experiment," *Journal of Geophysical Research*, Vol. 91, No. A9, 1986, pp. 9939–9946.

[7]Haerendel, G., "Alfvén's Critical Velocity Effect Tested in Space," *Zeitschrift für Naturforschung*, Vol. A, No. 37, 1982, pp. 728–735.

[8]Gavrilov, B. G., Podgorny, I. M., Sobyanin, D. B., Zetzer, J. I., Erlandson, R. E., Meng, C. I., Pfaff, R. F., and Lynch, K. A., "North Star Plasma-Jet Experiment Particles and Electric and Magnetic Field Measurements," *Journal of Spacecraft and Rockets*, Vol. 41, No. 4, 2004, pp. 490–495.

[9]Lynch, K. A., Torbert, R. B., Chutter, M., Erlandson, R. E., Meng, C. I., Zetzer, J. I., Gavrilov, B. G., and Kiselev, Y., "Active Plasma Experiment: North Star Particle Data," *Journal of Spacecraft and Rockets*, Vol. 41, No. 4, 2004, pp. 496–502.

[10]Delamere, P. A., Stenbaek-Nielsen, H. C., Pfaff, R. F., Erlandson, R. E., Meng, C. I., Zetzer, J. I., Kiselev, Y., and Gavrilov, B. G., "Dynamics of the Active Plasma Experiment North Star Artificial Plasma Jet," *Journal of Spacecraft and Rockets*, Vol. 41, No. 4, 2004, pp. 503–508.

[11]Gatsonis, N. A., DeMagistris, M., and Erlandson, R. E., "Three-Dimensional Magnetohydrodynamic Modeling of Plasma Jets in North Star Space Experiment," *Journal of Spacecraft and Rockets*, Vol. 41, No. 4, 2004, pp. 509–520.

[12]Kelley, M. C., Baker, S. D., Holzworth, R. H., Argo, P., and Cummer, S. A., "LF and MF Observations of the Lightning Electromagnetic Pulse at Ionospheric Altitudes," *Geophysical Research Letters*, Vol. 247, No. 9, 1997, pp. 1111–1114.

[13]Wescott, E., Stenbaek-Nielsen, H. C., Hallnan, T., Deehr, C., Romick, J., Olson, J., Kelley, M. C., Pfaff, R., Torbert, R. B., Newell, P., Foppl, H., Fedeer, J., and Mitchell, H., "Plasma-Depleted Holes, Waves, and Energized Particles from High-Altitude Explosive Plasma Perturbation Experiments," *Journal of Geophysical Research,* Vol. 90, No. A5, 1985, pp. 4281–4298

[14]Kintner, P. M., Kelley, M. C., Holmgren, G., and Bostrom, R., "The Observation and Production of Ion Acoustic Waves During the Trigger Experiment," *Journal of Geophysical Research*, Vol. 85, No. A10, 1980, pp. 5071–5077.

D. L. Cooke
Guest Editor

Color reproductions courtesy of NASA.